Comprehensive Summaries of Uppsala Dissertations
from the Faculty of Science and Technology 587

Magnetic Properties of Transition Metal Compounds and Superlattices

BY

ARVID BRODDEFALK

ACTA UNIVERSITATIS UPSALIENSIS
UPPSALA 2000

Dissertation for the Degree of Doctor of Technology in Solid State Physics presented at Uppsala University in 2000

Abstract

Broddefalk, A. 2000. Magnetic Properties of Transition Metal Compounds and Superlattices Acta Universitatis Upsaliensis. *Comprehensive Summaries of Uppsala Dissertations from the Faculty of Science and Technology* 587. 47 pp. Uppsala. ISBN 91-554-4860-7.

Magnetic properties of selected compounds and superlattices have been experimentally studied using SQUID (superconducting quantum interference device) and VSM (vibrating sample magnetometer) magnetometry, neutron diffraction and Mössbauer spectroscopy measurements combined with theoretical *ab initio* calculations.

The magnetic compounds $(Fe_{1-x}M_x)_3P$, M=Co or Mn have been studied extensively. It was found that Co can substitute Fe up to x=0.37. Increasing the Co content leads to a reduction of the Curie temperature and the magnetic moment per metal atom. Mn can substitute Fe up to x=0.25 while Fe can be substituted into Mn_3P to $1-x$=0.33. On the iron rich side, the drop in Curie temperature and magnetic moment when increasing the Mn content is more rapid than for Co substitution. On the manganese rich side an antiferromagnetic arrangement with small magnetic moments was found.

The interlayer exchange coupling and the magnetocrystalline anisotropy energy of Fe/V superlattices were studied. The coupling strength was found to vary with the thickness of the iron layers. To describe the in-plane four-fold anisotropy, the inclusion of surface terms proved necessary.

The in-plane four fold anisotropy was also studied in a series of Fe/Co superlattices, where the thickness of the Co layers was kept thin so that the bcc structure could be stabilized. Only for samples with a large amount of iron, the easy axis was found to be [100]. The easy axis of bulk bcc Co was therefor suggested to be [111].

Keywords: Magnetic order, magnetocrystalline anisotropy, interlayer exchange coupling, transition metal compounds, superlattices.

Arvid Broddefalk, Department of Materials Science, Uppsala University, Box 534, SE-751 21 Uppsala, Sweden

ISSN 1104-232X
ISBN 91-554-4860-7

Printed in Sweden by Eklundshofs Grafiska AB, Uppsala 2000

Till mina föräldrar

Allting har sin tid,
och varje företag
under himmelen har
sin stund.

Pre 3:1

List of papers

This thesis is based on the collection of articles given below. Each article will be referred to by its capital Roman numeral.

I. **Structural and magnetic properties of $(Fe_{1-x}Co_x)_3P$ compounds: experiment and theory**
Hui-ping Liu, P. James, A. Broddefalk, Y. Andersson, P. Granberg and O. Eriksson.
J. Magn. Magn. Mater. **189**, 69-82 (1998).

II. **Magnetocrystalline anisotropy of $(Fe_{1-x}Co_x)_3P$**
A. Broddefalk, P. Granberg, P. Nordblad, Hui-ping Liu and Y. Andersson.
J. Appl. Phys. **83**, 6980-6982 (1998).

III. **Structural and magnetic properties of $(Fe_{1-x}Mn_x)_3P$ (x <0.25)**
A. Broddefalk, P. James, Hui-ping Liu, B. Kalska, Y. Andersson, P.Granberg, P. Nordblad, L. Häggström and O. Eriksson.
Phys. Rev. B **61**, 413-421 (2000).

IV. **The antiferromagnetism of $(Fe_{1-x}Mn_x)_3P$, x ≥0.67, compounds**
Hui-ping Liu, Y. Andersson, P. James, D. Satula, B. Kalska, L. Häggström, O. Eriksson, A. Broddefalk and P. Nordblad.
In manuscript.

V. **Structural and magnetic properties of $TlCo_{2-x}Cu_xSe_2$, 0≤ x ≤1**
A. Broddefalk, P. Nordblad and R. Berger.
Physica B **284-288**, 1317-1318 (2000).

VI. **A study of the structural, magnetic and electronic properties of $TlCo_{2-x}Cu_xSe_2$**
R. Berger, M. Fritzsche, A. Broddefalk, P. Nordblad and O. Eriksson
In manuscript.

VII. **In-plane magnetic anisotropy of Fe/V (001) superlattices**
A. Broddefalk, P. Nordblad, P. Blomquist, P. Isberg, R. Wäppling, O. Le Bacq and O. Eriksson.
In manuscript.

VIII. **Interlayer exchange coupling and giant magnetoresistance in Fe/V (001) superlattices**
A. Broddefalk, R. Mathieu, P. Nordblad, P. Blomquist and R. Wäppling.
In manuscript.

IX. Structural and magnetic properties of bct Fe/Co (001) superlattices
P. Blomquist, R. Wäppling, A. Broddefalk and P. Nordblad.
In manuscript.

X. Magnetic moment arrangement in amorphous $Fe_{0.66}Er_{0.19}B_{0.15}$
B. Kalska, K. Szymanski, A. Broddefalk, R. Wäppling, P. Nordblad and L. Dobrzynski.
In manuscript.

The author has also contributed to the following papers, not included in the thesis

- **On the structural polymorphism of $CePt_2Sn_2$: experiment and theory**
  Hui-ping Liu, M. Colarieti-Tosti, A. Broddefalk, Y. Andersson, E. Lidström and O. Eriksson.
  J. Alloys Comp. **306**, 30-39 (2000).

- **μSR magnetic properties of stoichiometric and understoichiometric PrP**
  D. R. Noakes, R. Wäppling, G. M. Kalvius, Y. Andersson, A. Broddefalk, M. F. White Jr. and C. E. Stronach.
  Physica B **289-290**, 303-306 (2000).

Reprints were made with permission from the publishers.

Contents

Chapter 1

Introduction

Due to the complexity of magnetic materials and the large number of applications in which they can be used, a lot of research has been devoted to them. [1] Long range magnetic order is mainly found in materials which contains elements from the 3d transition metals (specially Fe, Co, Ni and Mn) and the 4f rare-earth metal series. Magnetic materials which contain 4f electrons usually have a saturation magnetisation close to that predicted from Hund's rules, but the moment configuration is quite often complicated and spin reorientations are often observed. The saturation magnetisation of the transition metals on the other hand very seldom follow Hund's rule and due to the itinerant nature of the 3d electrons, the saturation magnetisation can vary quite much. For applications, 3d materials are more often used due to their higher Curie temperatures. The materials are tailor-made to fit in the application. Whereas the coercivity has historically been the most important parameter, the growing interest of data storage has made the anisotropy and the magnetoresistive properties the most studied parameters.

There are several techniques to measure magnetic properties of a solid. The most straight forward method is to measure the magnetisation versus applied field, temperature or time. A lot of information can be deduced if the results can be interpreted properly. Magnetisation measurement is a global technique, where the total magnetisation is recorded. Other techniques are essential complements to get a more complete physical picture of a sample. In this thesis, magnetisation measurements have been complemented with neutron diffraction measurements, which give information about the moment configuration and the size of the individual moments, and Mössbauer spectroscopy measurements, which gives information about the internal fields of iron atoms. There are also other techniques, such as ferromagnetic resonance (FMR), torque magnetometry, x-ray circular magnetic dichroism (XMCD) and muon spin rotation (μSR) that give vital information about the magnetic properties of a sample. Recently magnetic imaging techniques such as magnetic force microscopy (MFM) have become more widely used, which has increased the understanding of e.g. magnetic domain patterns.

There is yet no complete model which covers all aspects of magnetism.

However, with the dramatic increase in speed of calculations made by computers, exceedingly complex problems can now be treated numerically with good accuracy. Band structure calculations have been able to solve old problems [2] as well as suggesting new phenomena for the experimentalists to verify [3]. Collaboration between experimentalists and theorists is thus important to increase the understanding of magnetism.

The samples studied in this thesis were chosen to be challenging for all participants in the projects, from chemists and film growers to the experimental and theoretical physicists. Several systems (iron phosphides, ternary transition metal selenides and Fe/V superlattices) also had historical connections to previous studies carried out in Uppsala. From magnetic perspectives, fundamental features were investigated. The critical temperature gives a measure of the coupling strength and the size of the magnetic moments is related to the size of the exchange splitting. These entities as well as the magnetic anisotropy energy are closely connected to the electronic structure of the material.

Chapter 2

Fundamentals

2.1 Thermodynamics

For a magnetic system, the appropriate thermodynamic potential is the Helmholtz free energy

$$F = U - TS. \tag{2.1}$$

For a given temperature, the system will configure the spins in such a way that the free energy is minimised. At high temperatures the entropy contribution will be dominant but at lower temperatures the free energy might be minimised by having an ordered spin state. The magnetisation is given by

$$M = -\frac{1}{\mu_0 V}\left(\frac{\partial F}{\partial H}\right)_T \tag{2.2}$$

and the susceptibility is

$$\chi = \left(\frac{\partial M}{\partial H}\right)_T. \tag{2.3}$$

For a ferromagnet, the order parameter is the *spontaneous magnetisation* which is non-zero below the critical temperature and zero above, as is shown in Fig. 2.1.

Most phase transitions from a paramagnetic to a ferromagnetic state is of second order. In that case, the susceptibility diverges at the critical temperature. The transition is described by the critical exponents, which depend on the spatial and spin dimensionalities of the system. For a review on phase transitions, see Ref. [4].

In some materials, e.g. ferromagnets and ferrimagnets, the magnetisation has a complicated dependence of the magnetic field. M is not a single-valued function of H and its value depends of the history of H. In addition, it will also depend on the sample shape.

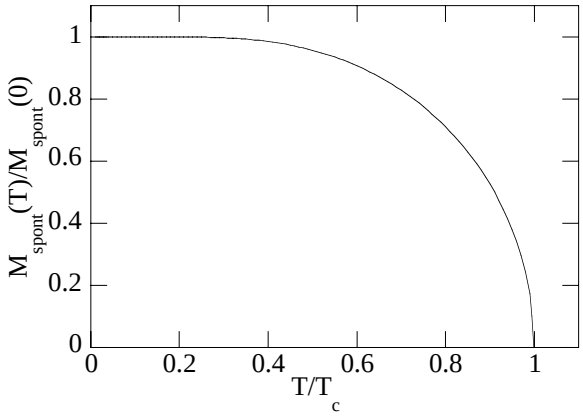

Figure 2.1: The zero-field magnetisation of a ferromagnetic domain. Below the critical temperature T_C there is a spontaneous magnetisation, M_{spont}.

2.2 Types of magnetic materials

All materials are magnetic. They are grouped according to how they respond to an applied magnetic field and to the magnetic structure if the material has any spin order. Filled electron shells have a negative response to H similar to Lenz's law. Materials that only consist of filled shells are called *diamagnetic* and the susceptibility is given by

$$\chi = -\frac{\mu_0 Z e^2 n < r^2 >}{6 m_e}, \tag{2.4}$$

where n is the number of atoms per unit volume, Z is the number of electrons per atom, e is the electronic charge, m_e is the electronic mass and $< r^2 >$ is the mean of the atomic radius squared. χ is essentially temperature independent for a diamagnet. Type I superconductors are perfect diamagnets below its critical field with $\chi \equiv$-1.

A *Langevin paramagnet* has at least one electron shell which is only partially filled. This will give rise to a magnetic moment $\vec{m}$. Generally, the magnetisation can be written

$$\vec{M} = \frac{1}{V} \sum \vec{m}, \tag{2.5}$$

which will sum to zero for a paramagnet in zero field since the moments are uncorrelated and no spontaneous magnetisation exists.

In ordered magnetic materials, an exchange interaction

$$w_{ij} = -2J \vec{m}_i \cdot \vec{m}_j \tag{2.6}$$

is aligning the moment i and j parallel if J is positive and antiparallel if J is negative. *Ferromagnets* have a positive J. If J is negative, adjacent moments are aligned antiparallel and the system can be divided into two sublattices with opposite magnetisation direction. If the sublattices have equal magnetisation the material is called antiferromagnetic. Otherwise it is called ferrimagnetic.

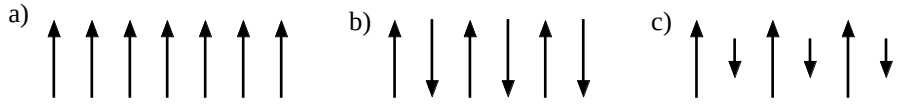

Figure 2.2: The main types of ordered magnetic structures. a) Ferromagnet b) Antiferromagnet c) Ferrimagnet

To model the behaviour of ordered magnets, the Hamiltonian is written [5]

$$\mathcal{H} = -2J \sum_{i>j} \left[a S_i^z S_j^z + b \left(S_i^x S_j^x + S_i^y S_j^y \right) \right], \tag{2.7}$$

where the summation is over nearest neighbours. For $a = b = 1$ we have the Heisenberg model which describes an isotropic system where the spins can rotate in three dimensions. For $a = 1$ and $b = 0$, the spins are either up or down. This is the Ising model. For $a = 0$ and $b = 1$ the spins will be constrained in the xy-plane, thus the name the XY model.

The cause of the exchange interaction is essentially the Pauli principle which acts due to the overlap of charge distributions. If two nearest neighbour magnetic ions have overlapping charge distributions it is called *direct exchange*. If the interaction is mediated by an intermediate non-magnetic ion the interaction is called *superexchange* and if the interaction is mediated by conduction electrons it is called *indirect exchange*. The different types of ordered spin configurations are shown in Fig. 2.2.

2.3 Models of magnetism

2.3.1 Localised model

When the unpaired electrons are localised near their native atom, their quantum state is described by the quantum numbers n, l, m_l, s, m_s. In a many electron system, the Russel-Saunders coupling applies in most cases. The atomic spin momentum S and orbital momentum L are formed by the sums of the respective angular momenta of the electrons within the atom. The total atomic angular momentum J is the sum of L and S. The atomic states are governed by Hund's rules, which tells that S should be maximised, L should be maximised and L is parallel to S if the shell is more than half full and antiparallel if the shell is less than half full.

The magnetic moment is then given by

$$m = -gJ\mu_B, \tag{2.8}$$

where

$$g = 1 + \frac{J(J+1) + S(S+1) - L(L+1)}{2J(J+1)} \tag{2.9}$$

is called Lande's splitting-factor and $\mu_B = e\hbar/2m_e$ is the Bohr magneton. For 3d elements in which the electrons still can be considered localised, e.g. in some oxides, the orbital moment is quenched. Then $J \approx S$ and $g \approx 2$.

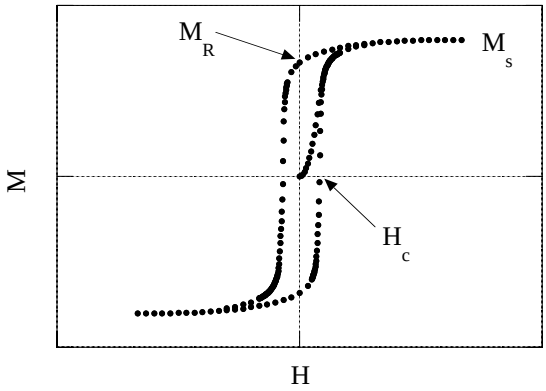

Figure 2.3: The typical field dependence of a ferromagnet. Important parameters are the saturation magnetisation M_s, remanent magnetisation M_R and coercivity H_c.

To calculate how a paramagnet behaves in a magnetic field, classical statistics can be used while remembering that the moments are quantised. The result is

$$M = NgJ\mu_B B_J\left(\frac{gJ\mu_B\mu_0 H}{k_B T}\right) \tag{2.10}$$

where N is the number of magnetic atoms per unit volume.

$$B_J(x) = \frac{2J+1}{2J}\coth\left(\frac{2J+1}{2J}x\right) - \frac{1}{2J}\coth\left(\frac{x}{2J}\right) \tag{2.11}$$

is called the Brillouin function. For small values of x the Brillouin function can be approximated as

$$B_J(x) = \frac{J+1}{3J}x. \tag{2.12}$$

Thus, for small values of H/T, the susceptibility of a paramagnet follows

$$\chi = \frac{N\mu_0 g^2\mu_B^2 J(J+1)}{3k_B T} = \frac{N\mu_0 m_{\text{eff}}^2}{3k_B T}, \tag{2.13}$$

where $m_{\text{eff}} = g\sqrt{J(J+1)}\mu_B$ is called the effective moment.

Ferromagnets have a complicated field dependence, see Fig. 2.3. The first try to explain the existence of ferromagnetism was done by Weiss. [6] The model included a molecular field $H_m = wM$ which aligns the moments. This model was later shown to be equivalent to taking the mean field approximation of the Heisenberg model, for details, see e.g. Ref. [7]. In addition to the molecular field, Weiss also introduced the concept of domains. Each domain is spontaneously magnetised to the saturation value, but the directions of the domains are in such a way that the total magnetisation is zero in zero field if the sample has no magnetic history. In applied fields the domains with directions parallel to the applied field grow at the expense of the other domains. This process is irreversible and causes the hysteresis. At a certain field the domain

walls are wiped out and only one domain exists, the magnetisation direction of which rotates with the magnetic field until saturation.

The temperature dependence of the spontaneous magnetisation within the Weiss model is given by the solution to Eq. (2.10) with the difference that H is changed to wM. At temperatures above the critical temperature, called the Curie temperature T_C, the susceptibility is given by

$$\chi = \frac{N\mu_0 m_{\text{eff}}^2}{3k_B(T-\theta_f)} \tag{2.14}$$

where

$$\theta_f = \frac{N\mu_0 m_{\text{eff}}^2 w}{3k_B}. \tag{2.15}$$

θ_f is called the asymptotic Curie temperature.

For an antiferromagnet with sublattices A and B, the molecular field for the A moments is given by $H_{mA} = w_{AA}M_A + w_{AB}M_B$, where w_{AB} is the inter-site interaction coefficient which is negative and usually much larger than the positive intra-site interaction w_{AA}. A similar expression can of course be written for the B sites. If $w_{AA} = w_{BB} = w_1$ and $w_{AB} = w_{BA} = w_2$ we end up with

$$\chi = \frac{N\mu_0 m_{\text{eff}}^2}{3k_B(T-\theta_a)} \tag{2.16}$$

where

$$\theta_a = \frac{N\mu_0 m_{\text{eff}}^2 (w_1+w_2)}{6k_B}. \tag{2.17}$$

The critical temperature, called the Néel temperature, is given by

$$T_N = \frac{N\mu_0 m_{\text{eff}}^2 (w_1-w_2)}{6k_B}. \tag{2.18}$$

More precise models define T_N at the maximum slope at temperatures just below the cusp. [8] the number of magnetic atoms The susceptibility below T_N is dependent on the angle between the applied field and the direction of the sublattice magnetisation. The typical behaviour of a uniaxial system (see section 2.4.1) is shown in Fig. 2.4. The field dependence for an antiferromagnet is free from hysteresis. It usually takes very large a field to reach saturation. If the field is applied parallel to the spins there could be a spin flop. At a certain field the energy is minimised by changing the spins to a configuration with the spins perpendicular to the applied field.

Ferrimagnets are similar to ferromagnets since they have a net moment and they are similar to antiferromagnets in the sense that the main interaction is negative. Néel divided ferrimagnets into different categories depending on the temperature dependence of the sublattices. [10] The most striking types are the P-type ferrimagnet which has an increasing net spontaneous moment at low temperatures and the N-type ferrimagnet for which the net spontaneous moment is zero at a point below the critical temperature.

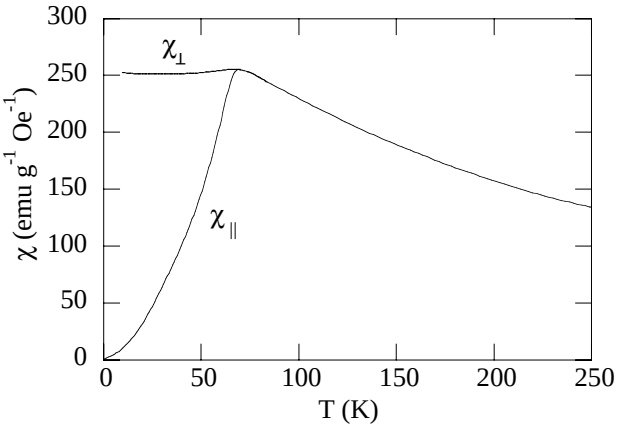

Figure 2.4: The temperature dependence of the mass susceptibility of MnF_2, which can be regarded as a typical uniaxial antiferromagnet. $\chi_{\parallel}$ and $\chi_{\perp}$ refer to the angle of the applied field with respect to the spins. (From Ref. [9])

The saturation magnetisation of ferromagnets are often much lower than expected from the localised model and are non-integers. For Fe, Co and Ni the moments should be 4, 3 and 2 μ_B, respectively, but turn out to be 2.2, 1.7 and 0.6 μ_B instead. For alloys of the 3d metals, the values of the saturation follow the Slater-Pauling curve, which is shown in Fig. 2.5. An interesting way to check to which extent the electrons of a ferromagnet are localised/delocalised is to look at P_c/P_s, where P_c is gJ deduced from M_s and P_s is gJ deduced from m_{eff}. For metals with low T_C the deviation may be large. [11]

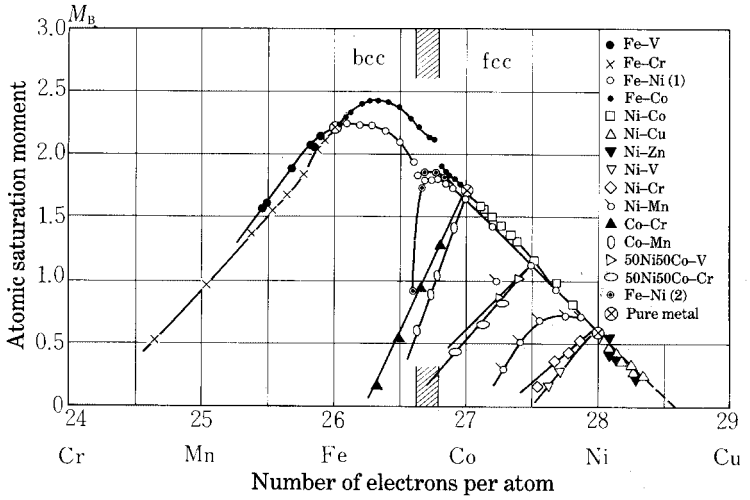

Figure 2.5: The Slater-Pauling curve. (After Bozorth. [15])

2.3.2 Itinerant model

When the electrons are completely delocalised from the atoms (itinerant) they can be described by their wave vector $\vec{k}$. In reality they also feel a periodic potential from the atom cores. Instead of energy levels, the important concept is now the bandstructure. Many physical properties of metals (and other solids) are related to this and to the density of states (DOS), $g(\epsilon)$, which is the number of states with a certain energy ϵ. Pauli [12] showed that in a magnetic field the DOS of the spin up electrons is shifted with respect to that of spin down electrons. Using the free electron model, this results in a positive temperature independent susceptibility $\chi = n_e \mu_0 \mu_B^2 / \epsilon_F$, when also the diamagnetic contribution due to a field induced orbital moment is taken into account. ϵ_F is the Fermi energy and n_e is the concentration of conduction electrons. Stoner suggested that if $Ig(\epsilon_F) > 1$, [13] the energy is lowered by a spontaneous split of the two spin channels. I is a parameter which is a measure of the exchange interaction, similar to the molecular field of the Weiss model. The total spin moment is just the difference between the number of spin up and spin down electrons (in units of Bohr magnetons). The itinerant model has proved to be good for calculating ground state properties of 3d magnets. Some techniques to calculate the bandstructure are described in section 3.4.

2.4 Anisotropy

2.4.1 Magnetocrystalline anisotropy

Besides the exchange energy that makes the moments tend to be parallel or antiparallel each other, there is an energy that makes the magnetisation direction lie along certain crystallographic directions, so called easy directions. This energy is called the magnetocrystalline anisotropy energy (MAE). The main cause of this energy term is the spin-orbit interaction $w = \lambda \vec{L} \cdot \vec{S}$. Even for 3d elements, there usually is some remaining unquenched orbital moment which couples the spin moment to some direction in space. MAE is expressed in terms of an expansion in direction cosines. The two most common types of anisotropy energies are cubic and uniaxial. For cubic systems it can be written

$$E_a^{\text{cubic}} = K_1(\alpha_1^2\alpha_2^2 + \alpha_2^2\alpha_3^2 + \alpha_3^2\alpha_1^2) + K_2\alpha_1^2\alpha_2^2\alpha_3^2 + \dots \tag{2.19}$$

where the α_i is defined through $\alpha_1 = \sin\theta\cos\varphi$, $\alpha_2 = \sin\theta\sin\varphi$ and $\alpha_3 = \cos\theta$. θ is the angle of the magnetisation to the z-axis and φ is the azimuthal angle. Whereas for a uniaxial system the MAE can be written

$$E_a^{\text{uniaxial}} = K_1 \sin^2\theta + K_2 \sin^4\theta + \dots \tag{2.20}$$

where θ is the angle of the magnetisation with respect to the unique axis.

The coefficients K_i govern the direction of the magnetisation. In uniaxial crystals, e.g. hexagonal or tetragonal, the direction of easy axis depends on K_i as is described in table 2.1 and Fig. 2.6a. For $K_1 > 0$ and $K_1 > -2K_2$ both an easy axis and an easy plane exist with a potential barrier between

Table 2.1: Preferred directions in a uniaxial crystal

Relations of K_i	Direction of magnetisation	E_a at easy direction
$K_1 > 0$	θ=0 (easy axis)	0
$K_1 < -2K_2$	$\theta = \frac{\pi}{2}$ (easy plane)	$K_1 + K_2$
$K_1 < 0, \quad K_1 > -2K_2$	$\theta \neq 0, \frac{\pi}{2}$ (easy cone)	$-\frac{K_1^2}{4K_2}$

them. The easy axis has the lower energy if $K_1 < -K_2$ and is metastable if $K_1 > -K_2$. The preferred directions are summarised in Fig. 2.6a. The cubic crystals always have either the cube edge, the body diagonal or in some few cases the face diagonal as easy axis yielding ranges of K_i according to table 2.2 and Fig. 2.6b.

A general rule is that cubic crystals have lower MAE than uniaxial crys-

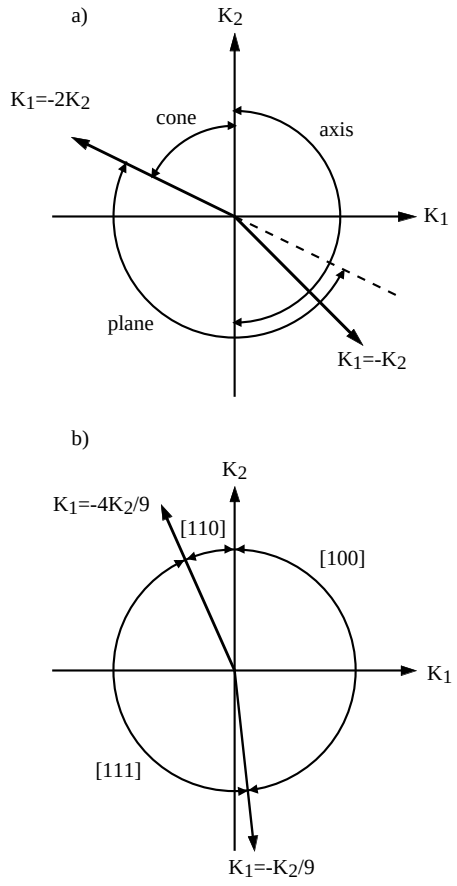

Figure 2.6: Preferred directions depending on the values of K_i for a uniaxial material (a) and cubic material (b).

Table 2.2: Preferred directions in a cubic crystal

Relations of K_i	Easy axis	E_a at easy axis
$K_1 > 0,\ K_1 > -\frac{1}{9}K_2$	[100]	0
$-\frac{4}{9}K_2 < K_1 < 0$	[110]	$\frac{1}{4}K_1$
$K_1 < -\frac{1}{9}K_2,\quad K_1 < -\frac{4}{9}K_2$	[111]	$\frac{1}{3}K_1 + \frac{1}{27}K_2$

tals due to the higher crystal symmetry. Furthermore, the anisotropy of 4f materials is larger than that of 3d materials since the orbital momentum is unquenched in 4f materials. For expansions including higher order terms of the anisotropy energies (see Ref. [14]), the uniaxial crystals cannot be treated with one common expansion but has to be treated according to the crystal symmetry. In most cases, higher order terms are t needed, and indeed, often the first constant is sufficient to describe the energy landscape rather well.

The anisotropy constants of a single crystal can e.g. be deduced from a magnetisation measurement. One usually then measures in two directions (the easy and a hard) and derives the enclosed area between the curves. This is a measure of the difference in E_a of the two directions. Another way to determine the anisotropy is to analyse the magnetisation curve measured along a hard axis. The energy caused by the field is $E_H = -\mu_0 \vec{M}_s \cdot \vec{H}$, which is called the Zeeman term. For magnetisation rotation, the energy is

$$E = E_a - \mu_0 H M_s \cos(\theta_0 - \theta), \tag{2.21}$$

where θ_0 is the angle between the field and the easy axis. This energy is minimised with respect to θ, which is the angle between the saturation magnetisation and the easy axis. This gives

$$H = \frac{dE_a/d\theta}{\mu_0 M_s \sin(\theta_0 - \theta)}. \tag{2.22}$$

The observed magnetisation is the projection of the saturation to the field direction,

$$M = M_s \cos(\theta_0 - \theta). \tag{2.23}$$

For a uniaxial crystal this turns out to

$$H = \frac{2K_1}{\mu_0 M_s^2} M + \frac{4K_2}{\mu_0 M_s^4} M^3 \tag{2.24}$$

in measurements perpendicular to an easy axis and to

$$H = \frac{-(2K_1 + 4K_2)}{\mu_0 M_s^2} M + \frac{4K_2}{\mu_0 M_s^4} M^3 \tag{2.25}$$

when measuring perpendicular to an easy plane. Cubic crystals have high symmetry and there are several possibilities of which angles to measure in. If [100] is easy and one measures in the [110] direction, there is no dependence on K_2 and

$$H = \frac{-2K_1}{\mu_0 M_s^2} M + \frac{4K_1}{\mu_0 M_s^4} M^3. \tag{2.26}$$

A table of $dE_a/d\theta$ for several possibilities of easy axes and directions of the magnetic field is given by Bozorth. [15] Some problems might occur when deducing the anisotropy using magnetisation curves. The angle of the field to the crystallographic axes has to be accurately set. Any misalignment will cause the field dependence of the magnetisation to change from the expected curve shape.

For a polycrystalline material it may still be possible to deduce the anisotropy constants from a magnetisation measurement since the magnetisation close to saturation is expected to follow

$$M = M_s \left\{ 1 - \frac{1}{2\mu_0^2 H^2 M_s^2} \left[\left(\frac{\partial E_a}{\partial \theta} \right)^2 + \frac{1}{\sin^2 \theta} \left(\frac{\partial E_a}{\partial \varphi} \right)^2 \right] \right\} \tag{2.27}$$

which for a polycrystalline uniaxial crystal turns out to

$$\begin{aligned} M &= M_s \Bigg\{ 1 - \frac{1}{15} \left(\frac{2K_1}{\mu_0 M_s} \right)^2 \left[1 + \frac{16}{7} \frac{K_2}{K_1} + \frac{32}{21} \left(\frac{K_2}{K_1} \right)^2 \right] \frac{1}{H^2} \\ &- \frac{2}{105} \left(\frac{2K_1}{\mu_0 M_s} \right)^3 \left[1 + \frac{16}{3} \frac{K_2}{K_1} + \frac{64}{11} \left(\frac{K_2}{K_1} \right)^2 + \frac{1024}{429} \left(\frac{K_2}{K_1} \right)^3 \right] \frac{1}{H^3} \Bigg\} \\ &= M_s \left(1 - \frac{b}{H^2} - \frac{c}{H^3} \right). \end{aligned} \tag{2.28}$$

Quite often other terms are included in this equation to improve the description of a real system. The problem is discussed by Grössinger. [16] The most common extra term is $-M_s a/H$, where a is an inhomogeneity parameter. Other methods to measure magnetic anisotropy are e.g. torque magnetometry [17] and FMR [18].

2.4.2 Shape anisotropy

The field dependence of the magnetisation of a ferromagnet will depend on the shape of the sample. This is due to poles on the surface that produce a demagnetising field opposite to the applied field. The internal field can be written as

$$\vec{H} = \vec{H}_{\text{applied}} - N\vec{M}. \tag{2.29}$$

N depends on the shape of the sample. It has the constraint $N_x + N_y + N_z = 1$. For a sphere $N_i = 1/3$, while for a infinite plane $N_x = N_y = 0$ and $N_z = 1$.

2.4.3 Magnetoelastic contributions

The strain dependence of the magnetic anisotropy energy can be expanded as

$$E_a = E_a^0 + \frac{\partial E_a}{\partial e_{ij}} e_{ij} + \frac{1}{2} \frac{\partial^2 E_a}{\partial e_{ij} \partial e_{kl}} e_{ij} e_{kl} + \ldots \tag{2.30}$$

where e_{ij} are the elements of the strain tensor. The first term corresponds to the anisotropy of the undistorted lattice. The second term represents the

magnetoelastic coupling, which for a cubic crystal may be expanded as

$$\begin{aligned} E_M &= B_1(\alpha_1^2 e_{xx} + \alpha_2^2 e_{yy} + \alpha_3^2 e_{zz}) \\ &+ 2B_2(\alpha_1\alpha_2 e_{xy} + \alpha_2\alpha_3 e_{yz} + \alpha_3\alpha_1 e_{xz}) + ldots \end{aligned} \tag{2.31}$$

Alternatively, in a known stress σ with direction cosines γ_i, the contribution is

$$\begin{aligned} E_M &= -\frac{3}{2}\lambda_{100}\sigma(\alpha_1^2\gamma_1^2 + \alpha_2^2\gamma_2^2 + \alpha_3^2\gamma_3^2) \\ &- 3\lambda_{111}\sigma(\alpha_1\alpha_2\gamma_1\gamma_2 + \alpha_2\alpha_3\gamma_2\gamma_3 + \alpha_3\alpha_1\gamma_3\gamma_1) + \ldots \end{aligned} \tag{2.32}$$

where λ_{100} and λ_{111} are the magnetostriction coefficients.

A slightly different expansion than Eq. (2.31), including higher order terms is described in Ref. [14], where also other symmetries are treated.

2.5 Properties of films and superlattices

The magnetic properties of thin films are different from those of the corresponding bulk sample. Several interesting features have been observed which are of fundamental as well as technological interest. Reducing the spatial dimension to two dimensions gives different critical temperatures and critical exponents. To obtain true 2D features, the films can only be one or two monolayers thick. Due to the lower symmetry at the surface, the size of the surface moments are altered in comparison to the bulk moments. For 3d elements the surface moment is generally enhanced since the reduced coordination leads to a narrowing of the d-band and an increased $g(\epsilon_F)$. At interfaces to magnetic metals, non-magnetic layers can get induced moments and ferromagnetic layers can get altered moments. To a good approximation, interface moments have been shown to follow the Slater-Pauling trend. [19]

Due to the shape anisotropy, the moments are expected to lie in the film plane. It has been seen in some cases that the moments instead are directed perpendicular to the film plane. Néel showed that a surface anisotropy appears when reducing the symmetry. [20] This anisotropy is uniaxial with the unique axis perpendicular to the film plane. It is also important that the in-plane anisotropy changes. Iron, for instance, has a surface anisotropy that favours [110] as easy axis, [21] which will compete with the bulk easy axis of [100]. When growing a film on a substrate, the lattice will experience tensile or compressive stresses. Due to the magnetoelastic coupling this might also contribute to out-of-plane anisotropy. du Trémolet de Lacheisserie [22] has derived adequate expansions of the magnetoelastic terms for films and superlattices made from cubic materials. These are given in accordance with tetragonal symmetry caused by the broken symmetry in the z-direction, but are for some reason seldom used. The strains might be quite large in a thin film and also the third term in Eq. (2.30), the morphic term, often contributes to the anisotropy. [23]

In practise, films cannot be grown without imperfections. Roughness will reduce the shape anisotropy, [24] steps will produce in-plane two-fold (uniaxial) anisotropies and terraces will modify the four-fold (quadratic) anisotropies. [25]

When forming a metallic superlattice, which consists of ferromagnetic and Pauli paramagnetic layers, the magnetic layers are often coupled through interlayer exchange interaction. The coupling energy per unit area S, between two ferromagnetic layers, denoted A and B, is usually expressed as

$$E/S = -J_{AB}\frac{\vec{M}_A \cdot \vec{M}_B}{M_s^A M_s^B}, \tag{2.33}$$

where J_{AB} is the interlayer exchange coupling (IEC) coefficient. The coupling has been found to oscillate with spacer layer thickness between ferromagnetically coupled (F) and antiferromagnetically coupled (AF) due to changes of sign in J_{AB}. [26] The effect can be described in terms of the quantum interference due to electron confinement in the spacer layer. [27] If the total energy of a superlattice is governed by AF coupling (J <0) and the Zeeman term, a minimisation leads to

$$J_{AB} = \frac{\mu_0 M_s H_{\mathrm{sat}} t_m}{4}, \tag{2.34}$$

where t_m is the thickness of the ferromagnetic layers.

The behaviour becomes more difficult to interpret if the anisotropy of the magnetic layers becomes comparable in size to the IEC. In addition, the coupling strength is also oscillating with the thickness of the magnetic layers. The amplitude is often small and the oscillation is not necessarily around J_{AB}=0. A multilayer is often covered with a capping layer to protect it from corrosion. This overlayer has also been shown to influence the coupling of the ferromagnetic layers in a multilayer. [28]

Non-collinear spin arrangements have been observed in multilayers. Special attention has been given the biquadratic coupling, where the moments of nearby layers align at 90^o. The cause of the non-collinearity between the layers is believed not to be intrinsic but to depend of defects [29] such as thickness variations or interdiffusion. It is however believed that multilayers of ferromagnetic and antiferromagnetic layers are able to form non-collinear structures without structural defects.

Of great interest for applications is the giant magnetoresistance (GMR) effect, [30] which is seen in superlattices of ferromagnetic and paramagnetic layers, in the antiferromagnetically coupled region. Magnetoresistance is the change in electrical resistance in an applied magnetic field. Magnetic metals show anisotropic magnetoresistance (AMR), which gives a different change if the field is applied parallel or perpendicular to the current direction. [31] The AMR effect is quite small, but still it has been used for sensors using permalloy as the AMR material. For AF coupled multilayers, a magnetic field will switch the layers to become oriented in parallel. The resistance in the ferro- and antiferromagnetic configurations might vary dramatically and the effect is called GMR. The GMR ratio is defined in two ways, either $[R(H=0) - R(H=H_s)]/R(H=H_s)$ or $[R(H=0) - R(H=H_s)]/R(H=0)$. The first definition is most commonly used. A typical measurement is seen in Fig. 2.7.

The GMR effect is due to spin dependent scattering in interfaces and in the bulk of the layers. The effect has both intrinsic (scattering at perfect interfaces

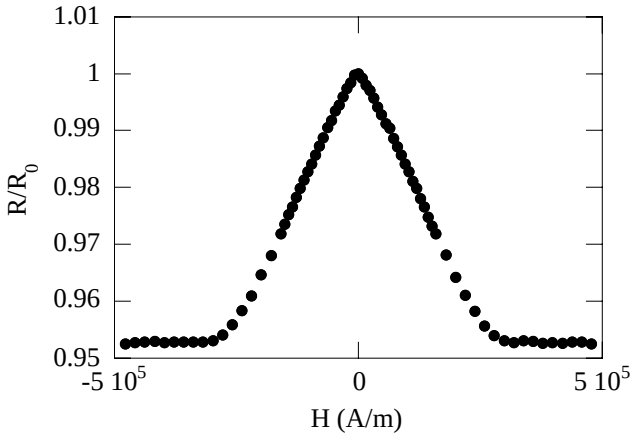

Figure 2.7: A typical GMR curve. There is no further reduction of the resistance once the applied field has aligned the spins.

due to band mismatch) and extrinsic (scattering by imperfections) origins. [32] The interface resistance can be written

$$r_{\uparrow(\downarrow)} = 2\,(1 \mp \gamma)\, r_b^* \tag{2.35}$$

and the bulk resistivities can be written

$$\rho_{\uparrow(\downarrow)} = 2\,(1 \mp \beta)\, \rho_F^*, \quad \rho_{\uparrow(\downarrow)} = 2\rho_N^* \tag{2.36}$$

β and γ are the spin asymmetry coefficients of bulk and interface scattering, respectively and F and N refers to the ferromagnetic and Pauli paramagnetic layers, respectively. For the case of a usual multilayer, the GMR ratio is positive, but if consecutive ferromagnetic layers have different signs of spin asymmetries, the ratio becomes negative and the effect is called inverse GMR. Alloys that follow the main line of the Slater-Pauling curve (Fig. 2.5) have positive β while alloys which follow the branches have negative values of β. Interfaces of ferromagnet/Cu have positive γ while most interfaces of ferromagnet/Cr have negative γ. In studies of GMR, two main geometries for the current transport are used, either with the current in-plane (CIP) or perpendicular to the film plane (CPP). The GMR ratio is different in these geometries due to different characteristic length scales. For CIP it is the mean free path that is of interest which causes the bulk scattering to be of less importance, but for CPP it is the much longer spin diffusion length. Thus, for systems where the bulk scattering is important for CPP, the two different geometries might give different signs of the GMR ratio. [32, 33]

Although the discovery of the GMR effect is rather recent, [34] it is already in use in sensor applications. In these sensors, superlattices are not used but so called spin-valve structures which consist either of a trilayer with two ferromagnets with different coercivities (such as cobalt and permalloy) or of two uncoupled magnetic layers where one is exchange coupled with an antiferromagnetic layer (usually FeMn). For these structures, the GMR ratio is lower

but the saturation field is much lower, making these structures good materials for use in e.g. read heads.

Recently, much attention has been devoted to tunnelling magnetoresistance (TMR) [35] where spin dependent tunnelling through an insulating interlayer occurs and also to colossal magnetoresistance (CMR), observed in certain manganites, where the magnetic phase transition is accompanied by a metal-insulator transition. [36]

Chapter 3

Experimental and calculational techniques

3.1 Magnetisation measurements

In the work presented here, most of the magnetisation measurements were carried out in a Quantum Design MPMS 5.5T SQUID magnetometer (SQUID: superconducting quantum interference device [37]) where the temperature can be varied between 1.7 and 400 K and the maximum applied field is $4.4 \cdot 10^6$ A/m. For measurements at higher temperatures a VSM (VSM: vibrating sample magnetometer [38]) equipped with a furnace, which makes measurements from room temperature to about 1000 K possible, was used. The maximum applied field is about $1.2 \cdot 10^6$ A/m in this setup.

The isothermal magnetisation measurements of different magnetic systems have been discussed in the previous sections, where the hysteresis effects and the law of approach to saturation were discussed. In this section the temperature dependence will be treated.

A ferromagnet has a true phase transition only in zero applied field. In order to get a non-zero magnetisation an applied field is necessary. Still, the critical temperature can be estimated from magnetisation measurements since the moments in each domain become uncorrelated at T_C which results in a drop in the magnetisation. Below the critical temperature, the magnetisation will be limited by the demagnetisation factor of the sample and by the intrinsic anisotropy. There are approaches within the mean field model of how to find the critical temperature from magnetisation measurements. Arrot has suggested to plot H/M vs M^2 for different isothermal measurements. [39] If the curve goes through the origin, the measurement was done at the critical temperature.

An important way to investigate the temperature behaviour of a magnetic system is to compare the magnetisation after having cooled the sample in zero field (ZFC) and after having cooled it in the measurement field (FC). In the ZFC, the sample is cooled to the lowest temperature, where the field is applied and the magnetisation is recorded while heating.

Where the ZFC/FC curves are split, irreversible magnetisation processes are present. An antiferromagnet with perfect compensation of the spins should show no difference between the ZFC and FC curves. However, any imbalance between the two sublattices, caused by e.g. defects or impurities gives rise to a split between the ZFC and FC curves at and below T_N. Also intended substitutions or dilution of the magnetic constituents give rise to a ZFC/FC split. A nice example of this is seen in Ref. [40].

3.2 Neutron diffraction

In neutron scattering experiments, there may be different types of scattering taking place. There is elastic and inelastic scattering, in which the energy and momentum is conserved in the first type and not in the second. There is coherent and incoherent scattering. Coherent scattering corresponds to Bragg scattering, while the incoherent scattering is a sort of background scattering. The condition for constructive interference is given by Braggs law

$$2d\sin\theta = \lambda \tag{3.1}$$

where d is the distance between the lattice planes and λ is the wavelength of the neutron. An important property of neutrons is that they carry a moment of -$\gamma\mu_N$, where γ=1.913 and $\mu_N = e\hbar/2m_p$ is the nuclear magneton. This means that there will be scattering both from the nucleus and from the atomic moments of the sample. For the case of unpolarised neutrons, the intensity will be proportional to the sum of the squared structure factors, (see e.g. Ref. [41])

$$\begin{aligned} I &\propto F^2_{\text{nucl}} + q^2 F^2_{\text{magn}} \\ &= \left|\sum b \exp\left[2\pi i\left(\frac{hx}{a_0}+\frac{ky}{b_0}+\frac{lz}{c_0}\right)\right]\right|^2 e^{-2W} \\ &+ q^2\left|\sum p \exp\left[2\pi i\left(\frac{hx}{a_0}+\frac{ky}{b_0}+\frac{lz}{c_0}\right)\right]\right|^2 e^{-2W} \end{aligned} \tag{3.2}$$

b is the scattering length, which is element specific and varies in an irregular manner with the atomic weight of the scattering element.

$$p = \left(\frac{e^2\gamma}{2mc^2}\right) gJf, \tag{3.3}$$

where f is the magnetic form factor which rapidly decreases with $(\sin\theta)/\lambda$.

$$\vec{q} = \vec{\epsilon}(\vec{\epsilon}\cdot\vec{K}) - \vec{K}, \tag{3.4}$$

where $\vec{K}$ is a unit vector in the direction of the atomic magnetic moment and $\vec{\epsilon}$ is the scattering vector, which is a unit vector in the direction perpendicular to the reflecting planes. If the angle between ϵ and K is denoted α it is seen that $q^2 = \sin^2\alpha$, which means that if the moment is perpendicular to the reflecting plane, no magnetic contribution to the intensity is seen. e^{-2W} is

the Debye-Waller factor, that reduces the amplitude at finite temperatures. When the magnetic unit cell is different from the structural unit cell, as in most antiferromagnetic materials, new diffraction peaks corresponding to the magnetic cell will appear. For ferromagnetic samples additional intensities will be seen on the crystallographic peaks since the two cells coincide. For powders, the spin direction is not easily obtained. For cubic materials it cannot be obtained at all and for uniaxial systems, only the angle between the spin and the unique axis can be obtained. For single crystals, the complete spin configuration can be obtained even for multidomain samples. [42]

3.3 Mössbauer spectroscopy

Mössbauer spectroscopy is a technique which gives detailed information of a certain isotope of the sample, most commonly ^{57}Fe. In that case a source of ^{57}Co decays to^{57}Fe. The γ-photons corresponding to the 3/2-1/2 transition in ^{57}Fe is selectively absorbed in an ^{57}Fe containing sample and the remaining photons are counted. The source is vibrated to Doppler modulate the photon energy to accommodate a full spectrum. There is a probability f that the photon is emitted and absorbed without recoil. From the spectrogram there are several physical properties that can be deduced. In a magnetic state, an iron site will give rise to a sextet. From the size of the splittings of the levels, the internal field can be deduced, which is the sum of the hyperfine field, the dipolar field and the external field. If the site is in a paramagnetic state, there will be a doublet if there is an electrical quadrupolar interaction present (which is caused by a non-spherical nucleus and a surrounding electric field gradient of low symmetry). In the magnetic case, this interaction can be seen as a perturbation which shifts the levels slightly. Another important parameter is the centroid shift (CS), which is the sum of the isomer shift (IS) and the second order Doppler shift (SOD). The IS is dependent of the concentration of the s-electrons in the nucleus. The SOD is a relativistic effect which is dependent on the Debye temperature of the sample. The velocity scale, and thus the CS, is usually given in reference to the room temperature spectrum of α-Fe.

The hyperfine field is of great interest, since it is proportional to the Fe moments. The hyperfine field is related to the Fermi contact which is proportional to the difference between concentration of the spin up and spin down s-electrons in the nucleus. The difference is due to differential attraction/repulsion to the unpaired 3d-electrons. When there are several Fe sites in the sample, the occupancy of them can be estimated from Mössbauer spectroscopy since the intensity of a given site is independent of the interactions and proportional to the number of ^{57}Fe in that type of site. For an easy to read introduction to Mössbauer spectroscopy, see Ref. [43].

3.4 Electron structure calculations

To calculate magnetic properties of a solid is indeed a difficult task. One approach is to investigate what happens at zero Kelvin using first principles calculations, which give the ground state properties of the system. The only input in the equations is the atomic number of the constituting atoms and the crystal symmetry of the system. This is done by finding an approximate solution to the Schrödinger equation.

$$\mathcal{H}\psi = E\psi. \tag{3.5}$$

Since the number of atoms in a system is very large, several approximations have to be imposed. The density functional theory (DFT) has been a powerful way to solve the problem, since the ground state energy is uniquely determined by the electron density $n(\vec{r})$. Kohn and Sham proposed a way to rewrite the problem into a single-particle problem, [44]

$$\left[-\nabla^2 + V_s(\mathbf{r})\right]\psi_i(\mathbf{r}) = \epsilon_i\psi_i(\mathbf{r}), \tag{3.6}$$

where

$$V_s(\mathbf{r}) = V_{\text{ext}}(\mathbf{r}) + \int d\mathbf{r}'\ \frac{2n(\mathbf{r}')}{\mid \mathbf{r}-\mathbf{r}' \mid} + V_{xc}[n(\mathbf{r})]. \tag{3.7}$$

The last term is the exchange-correlation potential determined by

$$V_{xc} = \partial E_{xc}[n(\vec{r})]/\partial[n(\vec{r})]. \tag{3.8}$$

To find this potential, $n(\vec{r})$ can be assumed to be slowly varying and then one obtains the local density approximation (LDA)

$$E_{xc} = \int n(\vec{r})\epsilon_{xc}[n(\vec{r})]d\vec{r}. \tag{3.9}$$

Approximate parametrisations of ϵ_{xc} are then used. The equations have to be solved self consistently. First a charge density is guessed. This gives a potential V_s after which the equation may be solved, resulting in a new charge density. These steps are iterated until the energy minimum is found. For a magnetic system, these calculations should be done for the two different spin channels, where the electron density is $n(\vec{r}) = n^{\uparrow}(\vec{r}) + n^{\downarrow}(\vec{r})$ and the magnetisation is $m(\vec{r}) \propto n^{\uparrow}(\vec{r}) - n^{\downarrow}(\vec{r})$.

There are some tools to aid the calculations. First of all, the calculations can be kept within small units in space. In most cases, the primitive cell is used but other units are also used, for instance, supercells are used when calculating properties of superlattices. Assumptions regarding the form of the basis functions are made. The wave functions are expanded in basis functions which are centered at the atomic centers. One type of expansion is the full potential linear muffin-tin orbital (FPLMTO) method. The wave functions are separated in two parts, one part within the muffin tin spheres and another one in the interstitial. Special functions are used in accordance to the symmetry of the problem.

Chapter 4

Systems

4.1 Chemically synthesized materials

4.1.1 $(Fe_{1-x}M_x)_3P$, M=Co or Mn

The Fe_3P structure is somewhat complicated (see Fig.4.1). It can be viewed as a distorted α-V_3S structure. [45] The structure is tetragonal with three different metal sites and eight formula units per unit cell. Fe_3P has been shown to be ferromagnetic with a critical temperature of about 700 K. From neutron diffraction, the individual moments have been found to be m_{Fe}(I)=2.12 μ_B, m_{Fe}(II)=1.25 μ_B and m_{Fe}(III)=1.83 μ_B at room temperature, where the moments essentially lie in the basal plane. [46]

In papers I-IV, the systems $(Fe_{1-x}M_x)_3P$, M=Co or Mn, have been studied. It was found that Co can be substituted up to x=0.37. Both the critical temperature and the 10 K saturation magnetisation were found to decrease with increasing Co content. There was a good agreement between the theoretically calculated values of the total moment with the experimental ones while the individual moments showed some small differences. The values of the moments were essentially determined by whether an Fe or Co atom occupied the site, i.e. no clear influence from the nearest neighbour surrounding was found.

The anisotropy constants of the polycrystalline $(Fe_{1-x}Co_x)_3P$ samples were found by measuring the high field magnetisation behaviour and using the law of approach to saturation. In order to account the demagnetisation influence of the magnetisation, the powders were sintered and formed to spheres, which have a known demagnetisation factor.

For $(Fe_{1-x}Mn_x)_3P$ the Mn could be substituted up to x=0.25 and Fe could be substituted into Mn_3P to $1-x$=0.33. For the iron-rich side, the critical temperature dropped much more rapidly than for the Co-substituted samples (see Fig. 4.2).

The saturation magnetisation decreased with increasing Mn content. The neutron diffraction, which observes the average value of a given site, gave decreasing moments with increasing x, while the Mössbauer spectroscopy gave the hyperfine field of iron at each site, which could be converted to Fe mo-

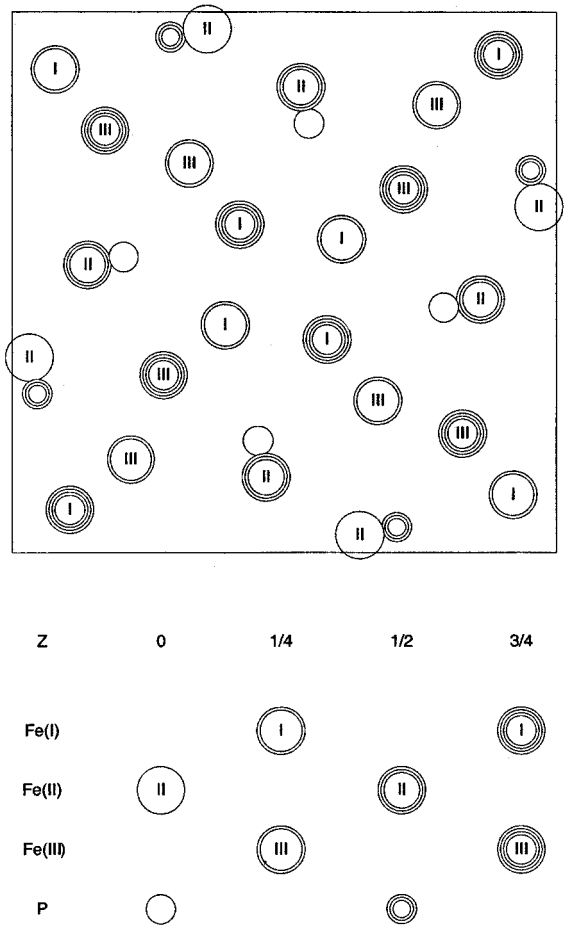

Figure 4.1: The Fe_3P crystal structure projected on the (001) plane.

ments. From these techniques it seemed that the Mn moments were aligned with the Fe moments, with relatively small Mn moments. Looking at the results from the *ab initio* calculations, which gave an increased total moment due to large Mn moments, the results were difficult to understand, since such calculations usually agree reasonably well with experiments. Two possible explanations were discussed. The Fe and Mn moments could be non-collinear. Then the decrease seen in the measurements would come from seeing a projection of the moments. The other possible explanation was that the Mn moments couple parallel or anti-parallel to the Fe moments depending on the number of Mn atoms in the surrounding. The results are summarised in table 4.1. Mn has been seen to arrange its moments in unconventional manners in several other compounds, and indeed in the Mn metal itself. Both explanations would suggest that the saturation magnetisation was underestimated from the magnetisation measurements.

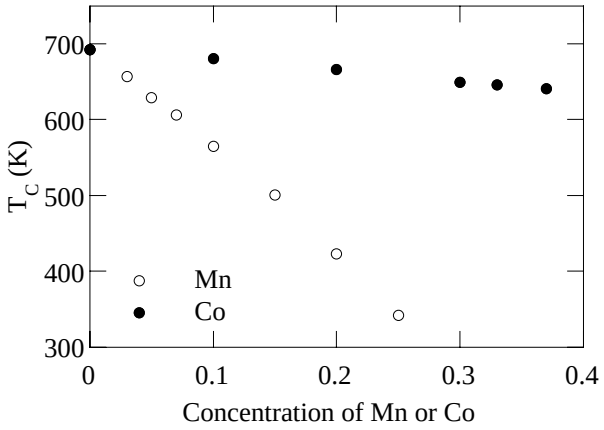

Figure 4.2: The Curie temperatures of $(Fe_{1-x}Co_x)_3P$, x <0.37 and $(Fe_{1-x}Mn_x)_3P$, x <0.25.

The manganese rich side also gave results that were difficult to understand. Magnetisation measurements on Mn_3P showed a weak bump at low temperatures which was attributed to antiferromagnetic ordering with a critical temperature of 35 K, which is quite far from the earlier reported Néel temperature of about 115 K. To complicate things, no new peaks or increased intensities in the neutron diffractograms were observed in comparison to those of higher temperature. Looking at the iron substituted samples, the magnetisation measurements showed similar behaviour as for Mn_3P, with critical temperatures that could be confirmed by Mössbauer measurements. These also showed that the iron moments were small, as is seen in Fig. 4.3. The neutron diffraction showed additional peaks for the iron substituted samples when comparing low and high temperature diffractograms. The critical temperature derived from the temperature dependence of the intensity of these peaks was in a good agreement with results from the other experimental techniques, see Fig. 4.4. The magnetic unit cell was found to be four times larger than the structural unit

Table 4.1: The total and individual moments of $(Fe_{1-x}Mn_x)_3P$. The moments are given in μ_B and the energy differences in mRy/metal atom. N: neutron diffraction. M: Mössbauer spectroscopy. VCA: virtual crystal approximation. In the calculations for x=0.33, one of the sites is fully substituted.

x		Site(I)	Site(II)	Site(III)	
0.15	occ. Mn	0.199	0.162	0.087	N
	m	1.96	1.26	1.92	N
	m_{Fe}	2.22	1.29	1.82	M
	m_{Mn}	0.9	1.1	2.9	N and M
0.10	m	2.54	1.57	1.92	VCA
0.33	$m_{\mathrm{Fe/Mn}}$	2.18	2.07	1.83	II subst.
	$m_{\mathrm{Fe/Mn}}$	2.47	1.55	1.84	I subst. (ΔE=+1.9)
	$m_{\mathrm{Fe/Mn}}$	2.14	1.49	2.26	III subst (ΔE=+2.4)

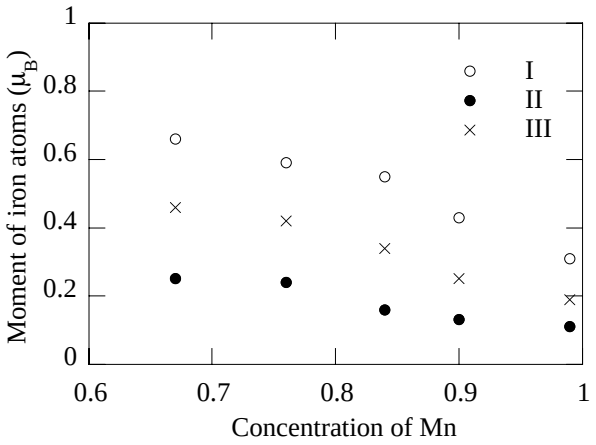

Figure 4.3: The iron moments of the three metal sites in $(Fe_{1-x}Mn_x)_3P$ deduced from Mössbauer spectroscopy.

cell, where the new a'-axis is $\sqrt{2}a$ along the [110] direction and the c'-axis is $2c$ along the [001] direction (a, c are the original unit cell axis). The additional peaks confirm the antiferromagnetic ordering of the compounds. Since the iron moments were small and decreasing with Mn content, one could speculate if the moments of pure Mn_3P sample are too small to be observed in the neutron diffraction experiments.

The first principles calculations gave two solutions of almost the same energy. The configuration of lowest energy of Mn_3P was the one with no moments, a Pauli paramagnetic solution. At a slightly larger energy the magnetic solution of lowest energy was antiferromagnetic with moments between 1.6 and 2 μ_B. The discrepancy of the sizes of the moments between theory and experiments was difficult to explain.

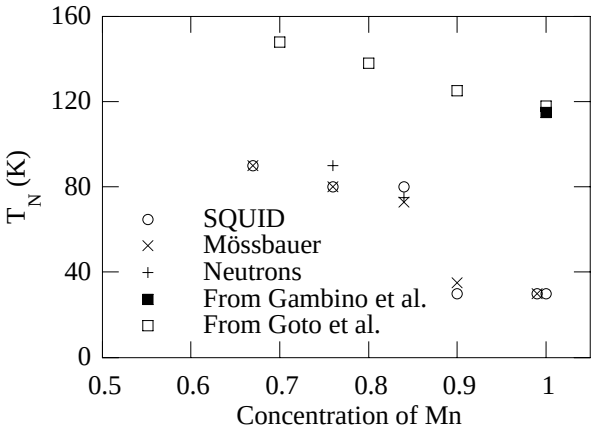

Figure 4.4: The critical temperatures of $(Fe_{1-x}Mn_x)_3P$, $x \geq 0.65$. The results of Gambino *et al.* [47] and Goto *et al.* [48] are also included.

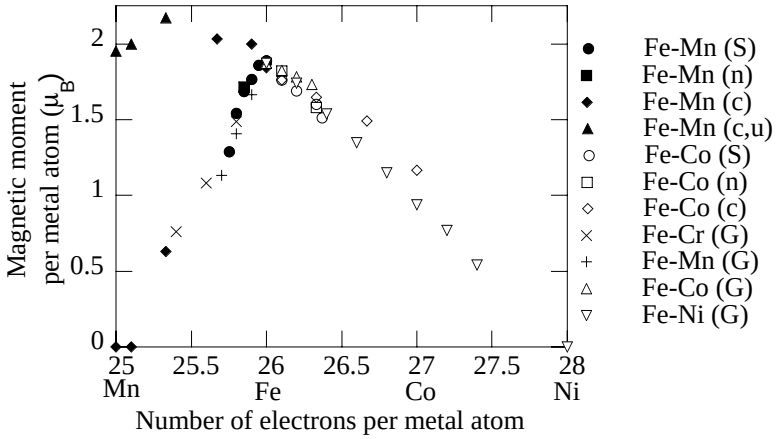

Figure 4.5: Magnetic moment per metal atom in $(Fe_{1-x}M_x)_3P$. The notations in the parenthesis denote from where the result was obtained. S: SQUID, n: neutron diffraction, c: *ab initio* calculations, u: unstable ferromagnetic solution, G: results from Goto *et al.* [48] (magnetisation measurements).

The magnetic moment per metal atom in $(Fe_{1-x}M_x)_3P$, M=Mn, Co, Cr and Ni is displayed in Fig. 4.5

4.1.2 $TlCo_{2-x}Cu_xSe_2$

$TlCo_2Se_2$ and $TlCu_2Se_2$ crystallise in the $ThCr_2Si_2$ structure, which is shown in Fig. 4.6. The Co atoms in $TlCo_2Se_2$ are found in layers in the structure. The intralayer distance between Co atoms is 2.7 Å while the interlayer distance is 6.8 Å. This large difference gives the sample a two-dimensional character, where the coupling in the layer is much stronger than coupling between the layers. Greenblatt *et al.* have examined a variety of substitutions on these ternary transition metal selenides. [49] $TlCo_2Se_2$ is antiferromagnetic with a T_N measured to 82 K for a single crystal and 97 K for a polycrystalline sample. The effective moment is 2.12 μ_B/Co atom. $TlNi_2Se_2$ is Pauli paramagnetic, while $TlCo_{2-x}Ni_xSe_2$ is antiferromagnetic up to x=1.5 with a maximum of T_N and m_{eff} at x=0.5, with the values T_N=142 K and m_{eff}=2.28μ_B/metal atom. $Tl_{1-y}K_yCo_2Se_2$ and $TlCo_2S_zSe_{2-z}$ showed ferromagnetism for $y \geq 0.55$ and $z \geq 1$, respectively. In quite many cases, the susceptibility below T_N showed peculiarities which were ascribed to a competition between ferromagnetic and antiferromagnetic interactions. The easy direction of the spins have been suggested to be in the *ab*-plane but the proofs are unconvincing. In an extensive study on $TlCu_{2-x}Fe_xSe_2$ also including $TlCoCuSe_2$ [50], it was seen that $TlCu_2Se_2$ is Pauli paramagnetic. $TlCoCuSe_2$ was found to have an orthorhombic structure, [50] but the magnetic properties were not studied. In order to investigate $TlCo_{2-x}Cu_xSe_2$ both powder and single crystal samples were prepared. For x <0.8, the susceptibility measurements showed antiferromagnetic features (an example is shown in Fig. 4.7), with a large difference between the curves measured parallel and perpendicular to the *c*-axis, while no anisotropy

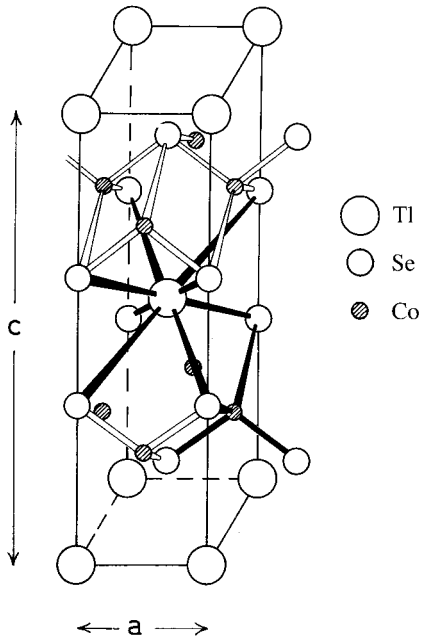

Figure 4.6: The crystal structure of $TlCo_2Se_2$.

in the *ab*-plane was observed. Increasing the Cu concentration leads to a lowering of the Néel temperature. The Curie-Weiss temperature was positive, which for a layered structure is an indication of a strong ferromagnetic intra plane coupling and a weaker inter plane coupling. *Ab initio* calculations on $TlCo_2Se_2$ showed that the antiferromagnetic solution with the spins in the *ab*-plane is the

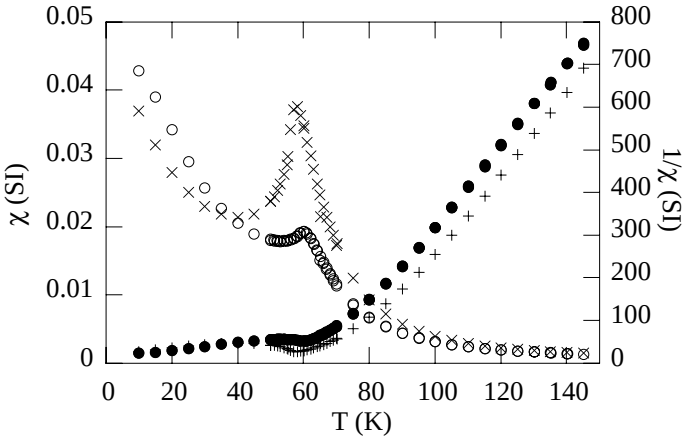

Figure 4.7: The temperature dependence of the susceptibility and the inverse susceptibility in 80 kA/m of $TlCo_{1.4}Cu_{0.6}Se_2$. $\circ : \chi \| c$, $\bullet : 1/\chi \| c$, $\times : \chi \perp c$ and $+ : 1/\chi \perp c$

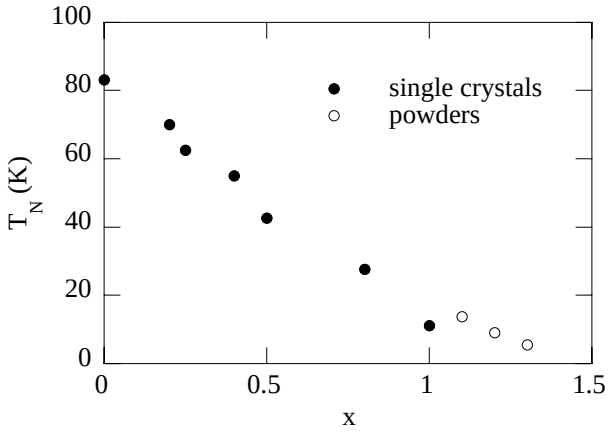

Figure 4.8: The critical temperatures of single- and polycrystalline $TlCo_{2-x}Cu_xSe_2$.

ground state. The moment of the cobalt atoms was found to be $1.45\mu_B$. Neutron diffraction measurements were undertaken on a powder $TlCo_2Se_2$ sample. The lattice parameter a showed a clear anomaly when passing through T_N, whereas the c-axis lattice parameter only continuously decreased. Below T_N two new peaks were observed at very low angles. These peaks could not be assigned to reflections of magnetic planes related to integer extensions of the c-axis. Helix structures appears in layered materials, where the interaction between nearest neighbour planes is ferromagnetic and the next-nearest neighbour planes have much stronger antiferromagnetic coupling. The in-plane spin direction is then varying from plane to plane in a spiral manner. In a neutron diffraction experiment, such spin structure yields satellites around the crystallographic peak. In the $TlCo_2Se_2$ case, it was not possible to assign the observed magnetic peaks to such a spin structure. The true spin structure in $TlCo_2Se_2$ thus remains an open question.

The orthorhombic structure was observed for $0.4 \leq x \leq 1.3$. In this range, the Cu and the Co atoms order structurally in an incommensurate manner. [51] In addition, a net moment is observed and the effective moment has a larger size.

4.2 Superlattices

4.2.1 Fe/V superlattices

Fe/V superlattices have been studied both theoretically and experimentally during the last two decades. It has e.g. been shown that Fe/V (001) superlattices can be grown with high quality by sputter deposition on MgO. [52] The epitaxial relationships for such multilayers are Fe/V(001) ∥ MgO(001) and Fe/V[110] ∥ MgO[100]. The in-plane matching to the substrate is made without too much strains since $a_{\mathrm{MgO}}/\sqrt{2}$=2.979 Å and the bulk values of the lattice

parameters of Fe and V are a_{Fe}=2.8664Å and a_{V}=3.0274Å, respectively.

X-ray results on sputtered films suggest excellent interfaces with roughness of only 1Å. [53] Magnetisation measurements on multilayers consisting of three or fewer monolayers of iron suggest inhomogeneous layers. [54, 55] For 3/14 samples, a GMR effect is observed at 300 K [55], while no magnetic spitting was observed above 133 K in Mössbauer experiments. [56] There is a rather wide distribution of hyperfine fields in the Fe layers when the V thickness is small. For superlattices where the V thickness is large, a large part of the iron atoms carry only very small hyperfine fields. The spatial distribution of moments in the iron layer of a 10/5 sample showed reduced moments compared to those of bulk iron even for the inmost layers.

It is found both from experiments and theoretical calculations that V gets an induced moment antiparallel to the nearby Fe layer. According to theoretical calculations, using bulk lattice parameters [57–60] or using the experimental lattice parameters as in paper VII, the V spin moment is of order 0.5 μ_B in the first layer whereas the subsequent layers have moments close to zero. X-ray magnetic circular dichroism (XMCD) on the other hand suggested that the total moment only slowly decays from an interface moment of 1 μ_B to about 0.3 μ_B at the tenth layer from the interface. [58, 61] Measurements of the g-factor [60, 62] support the theoretical results and also suggest that the Fe and V moments are coupled above T_C.

The anisotropy of Fe(N_{Fe} ML)/V(N_{V} ML) in the (001) geometry has been studied by Baberschke *et al.* for various combinations of N_{Fe} and N_{V}, where the thickness of the iron layers was small. [60, 62–65] All samples show in-plane easy direction. The in-plane anisotropy decreases when the thickness of the Fe layers decrease, but no spin-reorientation to [110] has been observed. Samples with $N_{\mathrm{Fe}} \leq 3$ show isotropic in-plane behaviour.

For Fe (15 ML)/V (1-12 ML) (001) superlattices, a strain dependent in-plane anisotropy was observed, [66] which is extensively analysed in paper VII. The anisotropy of the iron layers is modified due to the reduced symmetry of the surface atoms and the strain due to the in-plane matching of the lattice parameters of Fe and V. The way to analyse these modifications is to expand Eq. (2.30) in a tetragonal symmetry and compare the terms with an expansion in cubic symmetry. The strain dependence seemed linear (see Fig. 4.9) and the following expression was used to describe the behaviour:

$$\begin{aligned} \Delta E_a &= E_a[110] - E_a[100] = \frac{1}{4}(k_4^* + \frac{2}{t_m} k_{\mathrm{eff}}^s) \\ &+ \left\{ \frac{1}{12} \left[(B^{\alpha,4} + 2B^{\gamma,4})k + 2(B^{\alpha,4} - B^{\gamma,4}) \right] + \frac{2}{t_m} b_{\mathrm{eff}} \right\} \epsilon_{\parallel}, \quad (4.1) \end{aligned}$$

where k_4^* and $B^{\mu,4}$ are bulk cubic anisotropy and magnetoelastic coupling coefficients, respectively. k_{eff}^s and b_{eff} are the effective surface coefficients. t_m is the thickness of the magnetic layers, which in this case is 15 ML, k is the ratio between the out-of-plane and in-plane strains and $\epsilon_{\parallel}$ is the in-plane strain. Using values from the literature of the bulk coefficients, the effective surface contributions could be deduced. k_{eff}^s turned out to -28.3 μJ/m^2 and b_{eff}=-0.15 mJ/m^2.

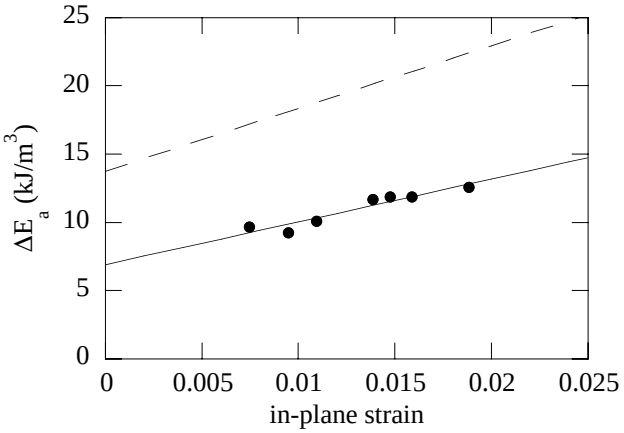

Figure 4.9: The obtained values of the anisotropy energy difference between [110] and [100]. Solid line: A linear fit of the experimental data points. Dashed line: The calculated behaviour for bulk iron.

The coupling of the Fe-layers is oscillating with the thickness of the V layers. Antiferromagnetic coupling peaks are observed at $t_V \approx 22$, 32 and 42 Å for the (001) geometry. [58] It can be argued that a first peak that is anticipated at 12 Å is suppressed by the transient ferromagnetic V moments. These moments are mainly coupled antiparallel to the Fe moments but a preference of the V moments to be parallel within a layer is also suggested. For thick V layers the second interaction is negligible, but for thin layers, the V moments at the two interfaces may interact also causing a ferromagnetic coupling of the Fe layers that overcomes the AF coupling.

The first peak in the AF coupling is extended between 12 and 16 ML of V. [55] The influence of the thickness of the Fe layer on the coupling and GMR ratio was studied in paper VIII. The magnetic properties of samples just outside the AF region was studied. Fe(3-13 ML)/V(11 ML) showed AMR with increasing amplitude corresponding to the increase observed for the in-plane magnetic anisotropy. For samples Fe(3, 5, 6, 9 and 13 ML)/V(13 ML), GMR was observed up to 9 ML of Fe. Superposed to this, AMR features were observed of similar magnitude as in the 11 ML V series. For the 13/13 sample, only AMR was observed. The antiferromagnetic coupling strength and the GMR ratio have maximum at 5-6 ML of Fe. Also varying the V layer thickness, it was seen that Fe(5 ML)/V(12-14 ML) had a maximum in coupling strength for 13 ML V.

lattice

4.2.2 bcc Fe/Co superlattices

An interesting feature of thin film growth is that structures that are unstable at ambient temperature and pressure can be stabilised by the influence of the substrate or the second constituent of a superlattice. For Co, the hcp structure is stable and fcc is metastable, while the bcc structure has been shown to be

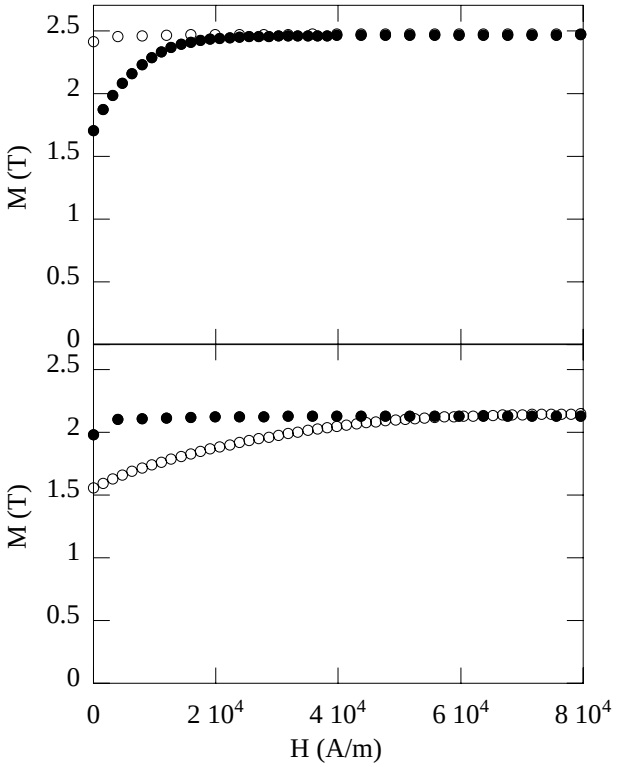

Figure 4.10: The magnetisation at 10 K of Fe (6 ML)/Co (2 ML) (top) and Fe (2 ML)/Co (6 ML) (bottom) when reducing the field from saturation to zero field in the [100] (○) and [110] (●) directions.

unstable. [67] Nevertheless, it has been shown to be possible to grow bcc Co in the ultrathin film limit. Most experimental work on bcc Co has been focused on samples grown on GaAs. The reported results on the magnetic properties have however been ambiguous. [68] The bcc structure of Co can also be achieved in Fe/Co superlattices on MgO (001) substrates, when the thickness of the Co layers is below 20 Å. [69]

In a series of Fe/Co (001) films, grown on MgO(001), the magnetic anisotropy and magnetic moments have been studied (see Paper IX). All samples showed in-plane four-fold anisotropy as is exemplified in Fig. 4.10. The easy direction is along the [100] direction for low Co content and crosses over to [110] at higher Co content in the films, see Fig. 4.11. I.e. there is a change in sign of the anisotropy constant at a Co content of 30 at.%. A change of sign in the first anisotropy constant when increasing the cobalt content has also been observed in FeCo alloys both in thin film and bulk form. [70] The magnetic moment of bcc Co has been extracted from magnetisation measurements on Fe/Co multilayers to $1.58\mu_B$ (when decomposing the magnetisation into Fe, Co and interface contributions [71]) and $1.71\mu_B$ (when extrapolating moments of a series of samples with constant Fe layer thickness, neglecting surface con-

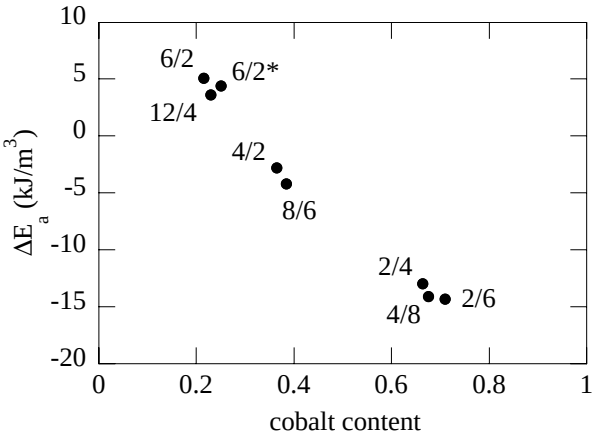

Figure 4.11: The anisotropy energy difference between [110] and [100] for all samples studied. $*$ denotes that the sample did not have the 100 Å Fe buffer layer.

tributions [72]), the latter being closer to theoretical values. [73] The moment profile of superlattices can be obtained from electron structure calculations and experimental techniques that measure the internal field. The magnetic moment profile at a bcc Fe/Co interface has been in debate. [19, 74] Results from perturbed angular correlation (PAC) measurements indicate oscillations in both Fe and Co moments through the interface, while *ab initio* calculations suggested an almost constant value for the Co moments but an increase of the Fe moments close to the interface. Recent Mössbauer studies have confirmed the calculated behaviour of the Fe moment at the interface. [75] The results of our magnetisation measurements is that Fe/Co superlattices have a larger total moment than the calculated summed moments of a corresponding Fe/Co interface.

4.3 Amorphous ribbons

Although amorphous solids do not have long range structural order, they can still show long range magnetic order if the magnetic elements have a large coordination number. If the material include magnetic transition metal and rare earth elements, the coupling between these are often negative, which leads to ferrimagnetic properties, where the different magnetic atoms form subnetworks similar to the sublattices of ferrimagnetic crystalline materials. The magnetisation direction of the atoms are also dependent on local anisotropies. Depending on the surroundings, easy and hard directions directions will appear that cause the 4f atoms to have a distribution of moment directions around the antiparallel configuration to the 3d atoms. This effect was observed in $Fe_{0.66}Er_{0.19}B_{0.15}$ (see paper X). Magnetisation curves at $8{\cdot}10^3$ and $8{\cdot}10^5$ are shown in Fig. 4.12. The behaviour is similar to that of an N-type ferrimagnet, [10] with a compensation temperature T_{comp} of about 120 K and a Curie temperature of 330 K.

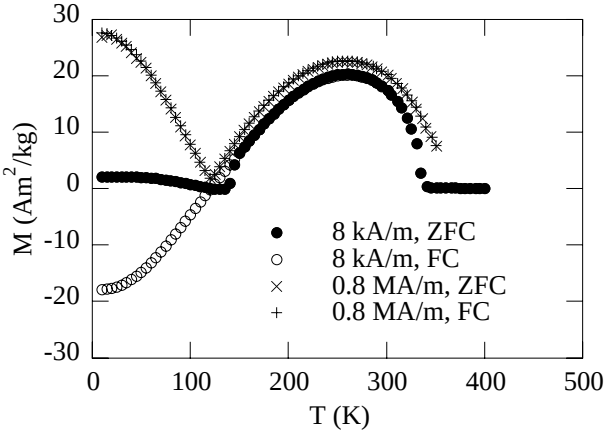

Figure 4.12: The ZFC and FC magnetisation of amorphous $Fe_{0.66}Er_{0.19}B_{0.15}$ in applied fields of $8{\cdot}10^3$ and $8{\cdot}10^5$ A/m.

At $8{\cdot}10^5$ A/m, the magnetisation gives a good measure of the net spontaneous magnetisation (except for temperatures close to T_{comp} and T_C), while the negative FC magnetisation in the $8{\cdot}10^3$ A/m measurement is due to the fact that the moments are locked in the high temperature configuration and when cooling below the compensation temperature, the field is too weak compared to the coercivity to flip the net magnetisation. Mössbauer spectroscopy measurements showed that the Fe subnetwork dominates at high temperatures, but due to a stronger temperature dependence of the Er subnetwork, Er dominates below T_{comp}. The Fe moments at low temperatures were from these experiments estimated to 1.55 μ_B which is lower than the value 2.2 μ_B of crystalline bcc Fe. This is expected from the fact that Fe is a weak ferromagnet with itinerant 3d orbitals. In a random surrounding the Fe moment is reduced. The projected Er moment to the direction antiparallel to Fe was derived by comparing results from Mössbauer and magnetisation measurements. The value of the Er moment at low temperatures ($6.9\mu_B$) is lower than the value expected from Hund's rules ($9\mu_B$). This is explained by introducing a distribution of directions of the Er moments. The exchange energy between the Fe and Er atoms will on average produce an antiparallel arrangement, but since local anisotropy energies are of the same order of magnitude as the exchange energy, the Er moments will show a distribution of angles to the antiparallel Fe moments.

Chapter 5

Acknowledgments

This work has been carried out at the Solid State Physics group at the Department of Technology (since 1 January 1997 the Department of Materials Science), Uppsala University, with financial support from the Swedish Natural Science Research Council (NFR) and Advanced Micro Engineering (AME).

I would like to thank my supervisors Per Nordblad (Stor-Per) and Per Granberg (Lill-Per) for excellent guidance and support. Much of the work has been done in collaboration with people from various groups of the Ångström laboratory, to all of whom I am also very grateful: Olle, Peter, Yvonne, Rolf, Ping, Lennart, Roger, Peter and Beata.

I would also like to thank the present and former members of the solid state physics group and especially: Olof, Peter, Mikkel, José, J-O, Johan, Malin, Claes, Johan, Ylva, Tomas, Kristian, Evie, Roland, Petra and Örjan.

could get.

Uppsala, 23 October 2000

Arvid Broddefalk

Bibliography

[1] S. Chikazumi, *Physics of Ferromagnetism*, 2nd ed. (Oxford University Press, Oxford, 1997).

[2] M. van Schilfgaarde, I. Abrikosov and B. Johansson, Nature **400**, 46 (1999).

[3] A. Taga, L. Nordström, P. James, B. Johansson and O. Eriksson, Nature **406**, 280 (2000).

[4] J. M. Yeomans, *Statistical Mechanics of Phase Transitions*, (Oxford University Press, Oxford, 1992).

[5] L. J. de Jongh and A. R. Miedma, Adv. Phys. **23**, 1 (1974).

[6] P. Weiss, J. de Physique, **6**, 661 (1907).

[7] A. Aharoni, *Introduction to the Theory of Ferromagnetism*, (Oxford University Press, Oxford, 1996).

[8] M. E. Fisher, Phil. Mag. **7**, 1731 (1962).

[9] S. Foner, J. Phys. Rad. **20**, 336 (1959).

[10] L. Néel, Ann. Phys. **3**, 137 (1948).

[11] R. R. Rhodes and E. P. Wohlfarth, Proc. Roy. Soc. **273**, 24 (1963); E. P. Wohlfarth, J. Magn. Magn. Mater. **7**, 113 (1978).

[12] W. Pauli, Z. Phys. **41**, 81 (1927).

[13] E. C. Stoner, Proc. Roy. Soc. A **165**, 372 (1938).

[14] E. du Trémolet de Lacheisserie, Ann. Phys. **5** 267 (1970).

[15] R. M. Bozorth, *Ferromagnetism* (van Nostrand, Princeton, 1951).

[16] R. Grössinger, Phys. Status Solidi A **66**, 665 (1981).

[17] H. Ziljstra, *Experimental methods in Physics. 2. Measurements of Magnetic Quantities*, ed. E. P. Wohlfarth (North-Holland, Amsterdam, 1967).

[18] M. Farle, Rep. Prog. Phys. **61**, 755 (1998).

[19] A. M. N. Niklasson, B. Johansson and H. L. Skriver, Phys. Rev. B **59**, 6373 (1999).

[20] L. Néel, J. Physique Rad. **15**, 225 (1954).

[21] J. G. Gay and R. Richter, Phys. Rev. Lett. **56**, 2728 (1986); B. Heinrich, Z. Celinski, J.F. Cochran, A.S. Arrott and K. Myrtle, J. Appl. Phys. **70**, 5769 (1991); M. Brockmann, S. Miethaner, R. Onderka, M. Köhler, F. Himmelhuber, H. Regensburger, F. Bensch, T. Schweinböck and G. Bayreuther, J. Appl. Phys. **81**, 5047 (1997).

[22] E. du Trémolet de Lacheisserie, Phys. Rev. B **51**, 15925 (1995).

[23] D. Sander, Rep. Prog. Phys. **62**, 809 (1999); M. Komelj and M. Fähnle, J. Magn. Magn. Mater. **220**, L8 (2000); M. Fähnle and M. Komelj, *ibid.* **220**, L13 (2000).

[24] P. Bruno, J. Appl. Phys. **64**, 3153 (1988).

[25] A. Moschel, R. A. Hyman and A. Zangwill, Phys. Rev. Lett. **77**, 3653 (1996).

[26] S. S. P. Parkin, N. More and K. P. Roche, Phys. Rev. Lett. **64**, 2304 (1990).

[27] P. Bruno, Phys. Rev. B **52**, 411 (1995); P. Bruno, J. Phys.:Condens. Matter **11**, 9403 (1999).

[28] A. Bounouh, P. Beauvillain, P. Bruno, C. Chappert, R. Mégy and P. Veillet, Europhys. Lett. **33**, 315 (1996).

[29] J. C. Sloncewski, J. Magn. Magn. Mater. **150**, 13 (1995).

[30] B. Dieny, J. Magn. Magn. Mater. **136**, 335 (1994); P. M. Levy, Sol. State Phys. **47**, 367 (1994).

[31] I. A. Campbell and A. Fert, *Ferromagnetic Materials*, E. P. Wohlfarth (ed.), vol. 3. (North-Holland, Amsterdam, 1982).

[32] C. Vouille, A. Barthélémy, F. Elokan Mpondo, A. Fert, P. A. Schroeder, S. Y. Hsu, A. Reilly and R. Loloee Phys. Rev. B **60**, 6710 (1999).

[33] S. Y. Hsu, A. Barthélémy, P. Holody, R. Loloee, P. A. Schroeder and A. Fert, Phys. Rev. Lett. **78**, 2652 (1997).

[34] M. N. Baibich, J. M. Broto, A. Fert, F. Ngyuyen Van Dau, F. Petroff, P. Etienne, G. Creuzet, A. Friederich and J. Chazelas, Phys. Rev. Lett. **61**, 2472 (1988).

[35] J. S. Moodera and G. Mathon, J. Magn. Magn. Mater. **200**, 248 (1999).

[36] J. M. D. Coey, M. Viret and S. von Molnar, Adv. Phys. **48**, 167 (1999).

[37] J. Clarke, Procedings of the IEEE **77**, 1208 (1989).

[38] S. Foner, Rev. Sci. Instr. **30**, 548 (1959).

[39] A. Arrott, Phys. Rev. **108**, 1394 (1957).

[40] P. Nordblad, Ö. Amcoff and T. Ericsson, Physica Scripta **60**, 373 (1999).

[41] G. E. Bacon, *Neutron diffraction*, 2nd ed. (Oxford University Press, Oxford, 1962).

[42] G. Shirane, Acta Cryst. **12**, 282 (1958); C. Wilkinson and E. J. Lisher, Acta Cryst. A **29**, 453 (1973).

[43] Tore Ericsson, *Mössbauer in Uppsala*, lecture notes.

[44] W. Kohn and L. J. Sham, Phys. Rev. **140**, A1133 (1965).

[45] S. Rundqvist, Y. Andersson and S. Pramatus, J. Sol. State Chem. **28**, 41 (1979).

[46] E. J. Lisher, C. Wilkinsson, T. Eriksson, L. Häggström, L. Lundgren and R. Wäppling, J. Phys. C **7**, 1344 (1974).

[47] R. J. Gambino, T. R. McGuire, and Y. Nakamura, J. Appl. Phys. **38**, 1253 (1967).

[48] M. Goto, H. Tange, T. Tokunaga, H. Fujii and T. Okamoto, Jap. J. Appl. Phys. **16**, 2175 (1977).

[49] G. Huan, M. Greenblatt and K. V. Ramanujachary, Sol. State. Comm. **71**, 221 (1989); A. R. Newmark, G. Huan, M. Greenblatt and M. Croft, *ibid.* **71**, 1025 (1989); G. Huan, M. Greenblatt and M. Croft, Eur. J. Sol. State Inorg. Chem. **26**, 193 (1989); G. Huan and M. Greenblatt, J. Less-Common Met. **156**, 247 (1989); M. Greaney, G. Huan, K. V. Ramanujachary, Z. Teweldemedhin and M. Greenblatt, Sol. State Comm. **79**, 803 (1991).

[50] R. Berger and C. F. van Bruggen, J. Less-Comm. Met. **113**, 291 (1985).

[51] L. Norén, R. L. Withers and R. Berger, J. Solid State Chem. **151**, 260 (2000).

[52] P. Isberg, Ph. D. thesis, Uppsala University (1997).

[53] P. Isberg, B. Hjörvarsson, R. Wäppling, E. B. Svedberg and L. Hultman, Vacuum **48**, 483 (1997).

[54] L.-C. Duda, P. Isberg, S. Mirbt, J.-H. Guo, B. Hjörvarsson, J. Nordgren and P. Granberg, Phys. Rev. B **54**, 10 393 (1996).

[55] P. Granberg, P. Isberg, E. B. Svedberg, B. Hjörvarsson, P. Nordblad and R. Wäppling, J. Magn. Magn. Mater. **186**, 154 (1998).

[56] B. Kalska, L. Häggström, P. Blomquist and R. Wäppling, J. Phys. Condens. Matter **12**, 539 (2000).

[57] R. Coehorn, J. Magn. Magn. Mater. **151**, 341 (1995).

[58] M. M. Schwickert, R. Coehorn, M. A. Tomaz, E. Mayo, D. Lederman, W. L. O'Brien, Tao Lin and G. R. Harp, Phys. Rev. B **57**, 13 681 (1998).

[59] J. Izquerido, A.Vega, O. Elmouhssine, H. Dreyssé and C. Demangeat, Phys. Rev. B **59**, 14 510 (1999).

[60] A. N. Anisimov, M. Farle, P. Poulopoulos, W. Platow, K. Baberschke, P. Isberg, R. Wäppling, A. M. N. Niklasson, and O. Eriksson, Phys. Rev. Lett. **82**, 2390 (1999).

[61] M. A. Tomaz, W. J. Antel Jr., W. L. O'Brien and G. R Harp, J. Phys.: Condens. Matter **9**, L179 (1997).

[62] M. Farle, A. N. Anisimov, K. Baberscke, J. Langer and H. Maletta, Europhys. Lett. **49**, 658 (2000).

[63] P. Poulopoulos, P. Isberg, W. Platow, W. Wisny, M. Farle, B. Hjörvarsson and K. Baberschke, J. Magn. Magn. Mater. **170**, 57 (1997).

[64] A. N. Anisimov, W. Platow, P. Poulopoulos, M. Farle, K. Baberschke, P. Isberg, P. Granberg and R. Wäppling, IEEE Trans. Mag. **34**, 873 (1998).

[65] A. N. Anisimov, W. Platow, P. Poulopoulos, W. Wisny, M. Farle, K. Baberschke, P. Isberg, B. Hjörvarsson and R. Wäppling, J. Phys.: Condens. Matter **9**, 10581 (1997)

[66] P. Granberg, P. Nordblad, P. Isberg, B. Hjörvarsson and R. Wäppling, Phys. Rev. B **54**, 1199 (1996).

[67] A. Y. Liu, and D. J. Singh, Phys. Rev. B **47**, 8515 (1993).

[68] Y. Z. Wu, H. F. Dong, C. Jing, D. Wu, G. L. Liu, V. Gordon, G. S. Dong, X. F. Jin, S. Zhu, and K. Sun, Phys. Rev. B **57**, 11935 (1998) and references therein.

[69] J. P. Jay, E. Jêdryka, M. Wójcik, J. Dekoster, G. Langouche and P. Panissod Z. Phys. B **101**, 329 (1996); B. Swinnen, J. Dekoster, J. Meersschaut, S. Demuynck, S. Cottenier and M. Rots, J. Magn. Magn. Mater. **156**, 71 (1996).

[70] Th. Mühge, Th. Zeidler, Q. Wang, Ch. Morawe, N. Metoki and H. Zabel, J. Appl. Phys. **77** 1055 (1995); R. C. Hall, J. Appl. Phys. **30**, 816 (1959).

[71] Ph. Houdy, P. Boher, F. Giron, F. Pierre, C. Chappert, P. Beauvillain, K. Le Lang, P. Veillet and E. Velu, J. Appl. Phys. **69**, 5667 (1991).

[72] J. Dekoster, E. Jedryka, M. Wójcik and G. Langouche, J. Magn. Magn. Mater. **126**, 12 (1993).

[73] D. J. Singh, Phys. Rev. B **45**, 2258 (1992) and references therein.

[74] B. Swinnen, J. Meersschaut, J. Dekoster, G. Langouche, S. Cottenier, S. Demuynck, and M. Rots, Phys. Rev. Lett. **78**, 362 (1997); Ž.V. Šlijvančanin, and F. R. Vukajlović, Phys. Rev. Lett. **80**, 1568 (1998); B. Swinnen, J. Meersschaut, J. Dekoster, G. Langouche, S. Cottenier, S. Demuynck, and M. Rots, Phys. Rev. Lett. **78**, 363 (1997).

[75] B. Kalska, P. Blomquist, L. Häggström and R. Wäppling, to appear in J. Magn. Magn. Mater.